CONF-790822--9

GA-A15487

MASTER

THERMAL ASPECTS IN THE DESIGN OF AN HTGR FUEL REPROCESSING PLANT

by

U-SUN PARK

AUGUST 1979

GENERAL ATOMIC COMPANY

DISCLAIMER

GA-A15487

THERMAL ASPECTS IN THE DESIGN OF AN HTGR FUEL REPROCESSING PLANT

by

U-SUN PARK

This is a preprint of a paper to be presented at the AIChE 87th National Meeting, August 19-22, 1979, at Boston, Massachusetts.

Work supported by
Department of Energy
Contract DE-AT03-76SF71053

GENERAL ATOMIC PROJECT 3261
AUGUST 1979

GENERAL ATOMIC COMPANY

THERMAL ASPECTS IN THE DESIGN OF AN HTGR FUEL REPROCESSING PLANT

U-Sun Park
General Atomic Company
San Diego, California

ABSTRACT

HTGR graphite-based spent fuel has been thermally analyzed to provide data for a reprocessing design. Steps include crushing, burning in fluidized beds, size classification, dissolution, and solvent extraction. The principal problem is that the bunkers holding feed and product between steps need sizing for decay heat. Constraints have been set for different modes of cooling. However, criticality may prove stricter.

Adverse effects of solvent degradation products in the Acid-Thorex process, mainly dibutyl phosphate (DBP), are reduced by using a partition flowsheet and by adding fluoride ions to the 1BX and 1CX columns.

INTRODUCTION

Commercial nuclear reactors use fuels that contain fissile and fertile materials, of which the latter is partially bred into a fissionable material during reactor operation. There are many incentives — economic, environmental, and resource conservation — to recover the unused and the bred fissile materials from the spent reactor fuels. The reprocessing of spent fuels from high-temperature gas-cooled reactors (HTGRs) is an even more significant part of the overall fuel cycle because of a higher conversion ratio compared to that of the light-water-cooled reactors (LWRs).

The HTGR, a helium-cooled thermal reactor, uses graphite as a fuel support structure as well as a moderator. A hexagonal graphite block (Fig. 1), which comprises more than 80% of a fuel element by weight, is loaded with approximately 1320 fuel rods. The fuel rods consist of fissile particles containing high- or medium-enriched U-235 and thorium oxide fertile particles bonded with carbonaceous matrix. Twenty-five percent of the fuel elements in the reactor core are replaced every year. The discharged spent fuel elements are cooled 180 days before they are reprocessed. Most of the fission products with a short half-life decay into more stable isotopes during the cooling period. The radioactivity and the rate of decay heat generation are still high after the 180 days of cooling, as shown in Table 1. As the fissile and the fertile particles are separated from the graphite fuel block and are concentrated during the process, the radioactivity and the decay heat generation per volume increase significantly in some parts of the process.

TABLE 1
SPENT HTGR FUEL DECAY HEAT GENERATION[a]

Particles	Crushed Fuel Elements	Fertile Kernel	SiC-PyC Coated Fissile Particles	Mixed Fuel Particles
Volume, cm^3/FE	103,000	1,860	1,900	3,760
Average decay heat rate, W/m^3	4,260	142.000	92,600	117,000
Maximum decay heat rate, W/m^3	6,380	213,000	139,000	176,000

[a]Assuming 4 years residence time in the HTGR core and 180 days cooling.

The purpose of this study is to investigate the effects of high radioactivity and decay heat generation associated with the spent fuel elements on the process and the equipment design in the HTGR fuel reprocessing plant; specifically: (1) constraints on the equipment sizing imposed by the decay heat generation, and (2) the effect of high radiation in the solvent extraction process, i.e., solvent degradation.

HTGR FUEL REPROCESSING PROCESS FLOW

Because a large quantity of graphite and pyrolytic carbons is present in spent fuel elements, a crush-burn-dissolution process has been developed and adopted as the reference head-end reprocessing step prior to a solvent extraction. The block flow diagram of the process is shown in Fig. 2.

The reprocessing process begins with crushing the hexagonal graphite fuel elements and burning them in a fluidized-bed combustor, freeing the fuel particles from the carbonaceous matrix fuel rods and removing particle coatings exterior to (fertile) particle kernels or silicon carbide coatings (fissile particles). The two types of particles are then separated by pneumatic classification based on differences in the particle size and the density. The burned-back thorium oxide fertile particles containing bred U-233 are dissolved and a purified uranyl nitrate solution is obtained by the Acid-Thorex solvent extraction process for transfer to refabrication. The burned-back fissile particles require additional crushing and burning to remove the silicon carbide and the underlying pyrocarbon coatings before dissolution and Purex or Thorex solvent extraction. The waste streams, gaseous, liquid, and solid wastes from the process, are treated separately for proper recycle, concentration, and storage.

The high radioactivity and the decay heat generation are associated with the fuel particles, and they affect the main process flow, which is indicated by the heavy lines in Fig. 2. In the solvent extraction process, most fission products are removed in the first extraction column (1A column) and sent to the high-level liquid waste storage before any further treatment. The head-end process prior to solvent extraction includes a series of material transfer and in-process interim storage of solid feed and products for all dry head-end systems, as shown in Fig. 3. Solid materials in

the interim storage exist in several different mixtures with different specific heat generation rates per volume. The average and the maximum decay heat rates from spent HTGR fuel elements are shown in Table 1. After 180 days cooling, the average decay heat generation rate is approximately 440 W/fuel element (1500 Btu/hr-FE), and the maximum decay heat rate is approximately 660 W/fuel element (2250 Btu/hr-FE). Approximately 60% of the decay heat comes from the fertile particles and approximately 40% comes from the fissile particles.

Bunkers are used for the in-process interim storage of solid particles. Because of the decay heat generation in the particle bunkers, temperatures in the bunkers may rise to excessively high levels unless adequate means of removing the heat generated are provided at the design stage. The effect of decay heat generation on other head-end systems is minimal because either the residence time is short in the system with a sufficient heat removal capacity or the process heat involved in some head-end systems, such as the fluidized-bed burners, is several orders of magnitude larger than the decay heat rate.

COOLING THE PARTICLE BUNKERS

The decay heat generated in the particle bunkers can be removed either internally or externally. In the present analysis, air, CO_2, and He cooling are considered. The simplest mode of cooling is that of free convection, in which heat is dissipated through the bunker wall into the cell ambient air. The heat load is, therefore, added to the HVAC system of the building. This mode of cooling is the simplest from the bunker design viewpoint. Forced convection cooling is another mode of external cooling. In this case, the particle bunkers are constructed as jacketed vessels with cooling air flowing through the jackets. A closed loop cooling system must be provided for the recirculation of cooling air. Internally, decay heat in the particle bunkers can be removed either by passing cooling gas through the particle beds or by insertion of internal cooling surfaces. The system incorporating internal cooling surfaces is inherently more complex and expensive to construct, and has the possibility of interference with particle flow. Direct contact cooling is, therefore, the only internal cooling mode considered in the present study. The three cooling modes are shown schematically in Fig. 4.

The allowable maximum temperature in the particle bunkers depends on the cooling gas and the solid material stored. It has been observed that no stable combustion takes place with graphite and pyrolytic carbons at bed temperatures below about 700°C. In the CO_2 atmosphere, consideration should also be given so that an excessive amount of CO will not be generated by the CO_2-carbon reaction,

$$CO + C \rightarrow 2CO$$

Examination of the equilibrium curve indicates that 600°C may be a practical temperature limit which corresponds to about 27% CO in an equilibrium mixture of CO_2-CO-C. In an inert gas atmosphere, such as He or Ar, the maximum temperature in the bunkers should not exceed the temperature above which particle agglomeration occurs. Preliminary investigation indicates that particle agglomeration takes place due to the formation of low melting point eutectics of alkali metal oxide, and SiO_2 from the SiC coating can lead to the formation of Cs_2O-SiO_2 eutectics, which have liquid phases at

870°C. The actual sintering temperature is not known at this time. For all the reasons above, 600°C has been chosen as the maximum allowable temperature in the particle bunkers. The results of this study, however, are applicable to other temperatures as well since the geometric constraints are represented graphically as a function of temperature.

Natural Convection Cooling

For a simple cylindrical geometry of the particle bunkers with a uniform heat generating source inside, the temperature distribution in the bunker can be obtained from the governing differential equation,

$$\rho_b C_p \frac{\partial T}{\partial t} = K_e \left(\frac{\partial^2 T}{\partial r^2}\right) + \left(\frac{1}{r}\frac{\partial T}{\partial r}\right) + Q \tag{1}$$

The solution of Eq. 1 with the following boundary conditions is given as

$$\text{B.C.} \begin{cases} T = T_w & \text{at} \quad r = R \\ \dfrac{\partial T}{\partial r} = 0 & \text{at} \quad r = 0 \end{cases}$$

$$T = T_w + \frac{QR^2}{4K_e}\left[1 - \left(\frac{r}{R}\right)^2\right] \tag{2}$$

At the outside of the bunker, heat is removed by ambient air such that at steady state:

$$h(2\Pi RL)(T_w - T_a) = (\Pi R^2 L)Q \tag{3}$$

or

$$T_w - T_a = \frac{QR}{2h} \tag{4}$$

Combining Eqs. 2 and 4, we get

$$T = T_a + \frac{QR}{2h} + \frac{QR^2}{4K_e}\left[1 - \left(\frac{r}{R}\right)^2\right] \tag{5}$$

The maximum temperature occurs at the centerline of the cylindrical packed bed, i.e., r = 0:

$$T_{max} = T_a + \frac{QR}{2h} + \frac{QR^2}{4K_e} \tag{6}$$

In order to use Eq. 6, the magnitudes of Q, h, and K_e must be known. Q is reasonably well predictable. The heat transfer coefficient from the cylinder wall to the ambient environment, h, is composed of two parts: h_c, the natural convection coefficient, and h_r, the radiation transfer coefficient.

$$h = h_c + h_r \tag{7}$$

For natural convection cooling of vertical cylinders in air (Ref. 1):

$$h_c = 0.19\ (T_w - T_a)^{1/3}, \quad \text{(for } 10^9 < (N_{Gr} \cdot N_{Pr}) < 10^{12}\text{, a condition applicable to the present analysis)} \tag{8}$$

The radiation transfer coefficient is also given by the following equation (Ref. 1):

$$h_r = \frac{0.171P\left[\left(\frac{T_w}{100}\right)^4 - \left(\frac{T_a}{100}\right)^4\right]}{T_w - T_a} \tag{9}$$

Combining Eqs. 4, 7, 8, and 9,

$$0.171\ P\left[\left(\frac{T_w}{100}\right)^4 - \left(\frac{T_a}{100}\right)^4\right] + (0.19)\ (T_w - T_a)^{4/3} = \frac{QR}{2} \tag{10}$$

Equation 10 gives T_w and h for a given Q at steady state.

Heat transfer in a packed bed is a complex phenomenon, and the effective thermal conductivity greatly depends on physical parameters such as bed voidage and particle diameter, as well as the intrinsic thermal properties of the materials involved such as the thermal conductivity of the solid particle and the interstitial gas used. Many available correlations predicting the effective thermal conductivity in a packed bed (Refs. 2-5), were compared with an experimental measurement done with a packed bed of pyrolytic carbon coated HTGR fuel particles in an He atmosphere at temperature ranges from 1000°C to 1500°C (Ref. 6). Agreement between the measured and predicted values was very good, and the Kunii-Smith correlation (Ref. 2) was adopted with a little simplification* for this study as follows:

$$\frac{K_e^o}{K_g} = \varepsilon\left(1 + \frac{h_{rv} d_p}{K_g}\right) + \frac{1 - \varepsilon}{\dfrac{1}{\dfrac{1}{\phi} + \dfrac{d_p h_{rs}}{K_g}} + \dfrac{K_g}{K_s}} \tag{11}$$

*This simplification predicts the value of K_e^o slightly higher than that without the simplification. The value is, however, still conservative. A recent experimental determination of the effective thermal conductivities with the actual fuel particles in the operating temperature range (Ref. 7) showed that the average measured thermal conductivities of the mixed fuel particles and the crushed fuel elements were twice as large as those predicted by Eq. 11. For the purpose of conservatism and in order to take the upper extreme values of the measurement (data scatter) into consideration, no attempt was made to modify the results of this study by using the measured values.

In case of small particles at relatively low temperatures, the radiation contribution can be neglected, and Eq. 11 reduces to:

$$\frac{K_e^o}{K_g} = \varepsilon + \frac{1-\varepsilon}{\phi + \frac{K_g}{K_s}} \tag{12}$$

The majority of the computations are, however, performed using Eq. 11. The predicted value of K_e^o is very sensitive to K_g and ε, as shown in Figs. 5 and 6, and is relatively less sensitive to K_s and d_p. A correct measurement or prediction of ε is, therefore, very important in designing the bunkers. For given physical parameters, the thermal conductivity of a packed bed, which determines the bunker size, can be improved markedly by using a gas with a higher thermal conductivity, such as He.

The bunker diameters for different maximum allowable temperatures in the bed and for different interstitial gases are shown in Figs. 7 and 8. Figure 9 shows the relationship between the decay heat rate and the maximum bunker diameter for the maximum allowable bed temperature of 600°C at steady state. The centerline temperature of the bunkers in Figs. 7 and 8 is the maximum bed temperature possibly attained by steady state. Normally, when a bunker is filled with new feed material, it takes time to develop the steady-state temperature distribution in the bunker. The transient temperature distribution analysis (Ref. 8) shows that the steady-state temperature in a crushed fuel element bunker is attained in several days after filling an empty bunker with fresh feed at ambient temperature, while it takes only a few hours for the mixed fuel particles.

Forced Convection Cooling

For a jacketed cylindrical vessel as shown in Fig. 4(b), the steady-state heat balance at the bunker wall gives:

$$h(T_w - T_g) = \frac{QR}{2} \tag{13}$$

Similarly, heat balance about the cooling air gives:

$$\frac{R_o^2 - R^2}{R^2} G C_{pg} \frac{dT_g}{dx} = Q \tag{14}$$

For simplicity, it is assumed that the heat loss to ambient air is insignificant. This should result in a conservative estimate of temperatures.

Equation 14 yields the following solution:

$$T_g - T_g^o = \frac{QR^2}{GC_{pg}(R_o^2 - R^2)} x \tag{15}$$

Combining Eqs. 13 and 15 gives:

$$T_w - T_g^o = \frac{QR}{2h} + \frac{QR^2}{GC_{pg}(R_o^2 - R^2)} x \tag{16}$$

Equation 2 still holds for the radial temperature distribution in the bunker. Combining Eqs. 2 and 16, we get

$$T - T_g^o = \frac{QR}{2h} + \left[\frac{QR^2x}{GC_{pg}\,(R_o^2 - R^2)}\right] + \left(\frac{QR^2}{4K_e}\right)\left[1 - \left(\frac{r}{R}\right)^2\right] \tag{17}$$

The maximum temperature at the centerline of the bunker, then, is given by:

$$T_{max} - T_g^o = \frac{QR}{2h} + \frac{QR^2L}{GC_{pg}\,(R_o^2 - R^2)} + \frac{QR^2}{4K_e} \tag{18}$$

Note that the temperature distribution is two-dimensional and the maximum temperature of the bed depends not only on the bunker radius but also on the bed height. The maximum bed temperature at the centerline occurs at the exit end of the bed.

With a convective heat transfer coefficient h, as given by McAdams (Ref. 1),

$$h = \left[\frac{C_{pg}\,G^{0.8}\mu_g^{0.2}}{(R_o - R)^{0.2}}\right]^{0.029} \tag{19}$$

typical temperature dependence on the bunker diameter for given values of $(R_o - R)$, L, and G is presented in Fig. 10. The maximum bed temperature can be controlled by adjusting either the bunker diameter or the bed height. For a given geometry, the maximum bed temperature decreases with an increasing cooling air mass velocity due to a higher heat transfer coefficient. This, however, soon reaches a plateau, and the bed temperature decreases only slightly with an increasing cooling air mass velocity when the slow heat conduction in the bed begins to control the rate of heat flow as shown in Fig. 11. The axial temperature distribution is linear (Eq. 17) both at the wall and at the center of the bed.

Internal Direct Cooling

In direct cooling, air is passed through the packed bed of particles to remove the decay heat generated. The steady-state heat balance leads to:

$$K_e\left(\frac{\partial^2 T}{\partial r^2} + \frac{1}{r}\frac{\partial T}{\partial r}\right) - ah_p(T - T_g) + Q = 0 \tag{20}$$

$$\frac{\partial T_g}{\partial x} + \left(\frac{ah_p}{GC_{pg}}\right)(T_g - T) = 0 \tag{21}$$

$$\text{Since}\quad \frac{\partial T}{\partial x} \cong \frac{\partial T_g}{\partial x} \tag{22}$$

Eqs. 20 and 21 can be combined to give:

$$K_e\left(\frac{\partial^2 T}{\partial r^2} + \frac{1}{r}\frac{2T}{\partial r}\right) - GC_{pg}\left(\frac{\partial T}{\partial x}\right) + Q = 0 \tag{23}$$

Eq. 23 can be solved with the following boundary conditions to yield (Ref. 8):

$$\text{B.C.} \quad -K_e \frac{\partial T}{\partial r} = h(T - T_a) \quad \text{at} \quad r = R, \; x \geq 0$$
$$T = T_o \quad \text{at} \quad x = 0, \; r \geq 0 \tag{24}$$

$$T(r,x) = \sum_{m=1}^{\infty} \left\{ \left(\frac{2T_o H}{R(H^2 + \beta_m^2)} \right) \left(\frac{J_o(\beta_m r)}{J_o(\beta_m R)} \right) \exp\left(-\alpha \beta_m^2 x\right) + \left[\left(\frac{2QH}{R(H^2 + \beta_m^2) K_e \beta_m^2} \right) + \left(\frac{2h\, T_a}{R(H^2 + \beta_m^2) K_e} \right) \right] \left(\frac{J_o(\beta_m r)}{J_o(\beta_m R)} \right) \left[1 - \exp\left(-\alpha \beta_m^2 x\right) \right] \right\} \tag{25}$$

where $$\alpha = \frac{K_e}{G C_{pg}} \tag{26}$$

$$H = \frac{h}{K_e} \tag{27}$$

$$\beta_m = \text{positive roots of } \frac{\beta J_1(\beta R)}{J_o(\beta R)} = H \tag{28}$$

Equation 25 has been computed for several cases by summing the first 100 terms of the infinite series using mean values of thermal conductivity and heat transfer coefficient. Figures 12 and 13 show the radial and axial temperature distributions, respectively, for a 305 mm (1 ft) diameter mixed fuel particle bunker. The wall cooling effect on the maximum temperature at the centerline is relatively insignificant until the bed height becomes very large. The maximum bed temperature is almost linear to the bed height as expected. As the bed diameter becomes large, the wall cooling effect becomes totally negligible as shown in Figs. 14 and 15, which present the radial and axial temperature distributions of a 915 mm (3 ft) diameter bunker containing crushed fuel elements, respectively. The results also show that the heat transfer between the particles and the cooling air is fast relative to the decay heat generation. In this case, for a relatively large diameter bed the maximum temperature at the center of the bed can be obtained by a simple heat balance between the gas and the decay heat generation instead of using Eq. 25. In all the calculations above, a cooling air mass velocity of 635 kg/m^2-hr was used, which corresponds to approximately the incipient fluidization velocity of the lighter fissile particles in the mixed particle bed. Increasing the air mass velocity beyond this point will lead to segregation of the fissile and fertile particles, a condition that is to be avoided. A further increase in air mass velocity, however, will eventually lead the bed to a fluidized state in which the particles are well

mixed and move freely in a suspended state. This results in a totally different type of cooling mode, which is discussed next.

The Fluidized State

In a vigorously fluidized bed (bubbling bed), the temperature of the particle bed is approximately uniform. Unlike direct internal cooling, the effect of radius (actually it is the surface area per unit volume ratio) on the equilibrium fluidized bed temperature is very significant, primarily due to its high heat transfer coefficient in the fluidized bed, as shown in Fig. 16.

With a loss in the fluidizing gas (as well as cooling gas), the bed settles to a packed bed and the case becomes identical to the transient case of the natural convection cooling. Upon restart, the bed undergoes a transient cooling before a thermal equilibrium state is reached. The heat balance during the transient gives:

$$\frac{dT}{dt} = \left(\frac{Q}{\rho_b C_p}\right) - \left(\frac{2h}{\rho_b C_p R}\right)(T - T_a) - \left(\frac{G\,C_{pg}}{\rho_b C_p L}\right)(T - T_g^o) \tag{29}$$

Equation 29 can be solved to give

$$T = T_o \exp\left(-\frac{2hL + G\,C_{pg}\,R}{\rho_b\,C_p\,RL}t\right) + \left(\frac{QRL + 2hT_a L + GC_{pg}\,T_g^o R}{2hL + GC_{pg}R}\right) \cdot \left[1 - \exp\left(-\frac{2hL + GC_{pg}R}{\rho_b\,C_p\,RL}\,t\right)\right] \tag{30}$$

Figure 17 shows the transient temperatures for three types of particle beds with the 152 mm (6 in.) diameter bed originally at 610°C fluidized with air vigorously at 3810 kg/m^2 • hr mass flow velocity. In all cases, it is seen that the bed temperatures reach equilibrium in about 2 hours.

SOLVENT DEGRADATION

The effect of decay heat generation by fission and activation products on the solvent extraction process in HTGR fuel reprocessing is a little different in nature from that on the head-end process. While in the latter the primary effect is the constraints in equipment sizing, the decay heat and the radiation in the solvent extraction process directly affect the process by radiochemical reactions. In all solvent extraction processes, including the Acid-Thorex process, more than 99% of the radioactive fission product nuclides in the feed stream are separated into the waste stream in the first cycle extraction column. Therefore, more than 99% of any solvent degradation due to radiation occurs in the first extraction (1A) column (Fig. 18), and we may neglect radiation degradation in other process equipment (Ref. 9).

The primary product of radiation degradation of tributyl phosphate (TBP) solvent used in the Acid-Thorex process is dibutyl phosphate (DBP), although monobutyl phosphate (MBP) is formed to a lesser extent. The extent of decomposition of TBP by radiation (usually represented by the G value, molecules of TBP changed per 100 electron volts absorbed) depends greatly on the total dose rate to the solvent. It is generally agreed that solvent radiation exposures of 0.5 watt-hr/ℓ will not significantly affect the

solvent performance. Adequate solvent washing will limit the cumulative effects of radiation, permitting accumulated doses of up to 20-45 watt-hr/ℓ with good solvent performance (Refs. 10, 11).

The extent of solvent degradation in the Acid-Thorex process has been studied at the lowest expected flowrates and highest specific activity (Ref. 12). In calculating the exposure received by the solvent during its contact with the aqueous feed in the column mixing zone, it can be conservatively assumed that all the α and β radiation is absorbed in the column if the column diameter is over 1 in. (Ref. 10). The fraction of γ radiation absorbed depends on the system geometry and the γ strength. Davis (Ref. 9) found 44% absorption in a 5-inch diameter column for short-decay Thorex runs. It is assumed that the average γ disintegration strength is 0.7 MeV. Combining the power density in the mixing section of the column and the residence time of solvent in the mixing section, the exposure of solvent during mixing is calculated. In addition, the solvent exposure to γ radiation from all in-cell sources was calculated. The conservatively estimated values for the fertile and fissile Fort St. Vrain reactor fuels and for the LHTGR fertile fuel are 0.48, 1.76, and 0.7 watt-hr/ℓ, respectively.

G values for pure TBP ranging from 1.5 to 2.44 have been reported by many investigators (Refs. 13, 14, 15). Using an average G value of 1.9, which appears conservative for a 30% TBP/NPH (natural paraffinic hydrocarbon diluent) system, the radiation decomposition of TBP under the estimated radiation dose above is on the order of 0.008 ~ 0.03% (Ref. 12). In terms of TBP losses, solvent degradation is trivial. However, enough DBP is formed using the 30% TBP flowsheet to cause the precipitation of thorium dibutyl phosphate. Solvent degradation in the Acid-Thorex process causes: (1) reduction in partitioning efficiency due to formation of an acid unstrippable thorium-DBP complex, (2) loss of fission product decontamination due to the formation of solvent-soluble DBP-fission product complexes, particularly zirconium, which reduces scrubbing effectiveness, (3) changes in phase dispersion characteristics in the uranium stripping (1C) column (Fig. 18) due to precipitation of thorium-DBP at lower stripping acidities, and (4) precipitation of thorium hydroxide in the solvent wash column on contact with the basic (sodium carbonate) wash solution.

The adverse effects above are remedied by introducing 0.005 M and 0.001 M, respectively, of fluoride ion to the partition (1BX) and the stripping (1CX) columns. Selective stripping of thorium results on contact of a solvent phase containing thorium-DBP complex with fluoride ion in an aqueous medium. GA pilot plant test results (Refs. 16, 17) showed that the desired lower thorium concentration in the partition (1BU) stream was achieved. The presence of fluoride in the 1BX stream improved thorium separation even when no DBP was present (Fig. 19). Thorium carryover from the 1C column to the solvent wash column was reduced by factors of 10 to 100 with fluoride in the 1CX versus no fluoride. No white precipitate (thorium hydroxide) formed at the interface as had occurred with no fluoride in the 1CX stream. The radiation effects observed by Richardson (Ref. 11) on the Purex system show a greater loss in Zr decontamination per unit of radiation damage (watt-hr/ℓ) than does the Acid-Thorex system as shown in Fig. 20. The reason for this observed difference is that the thorium ion forms a stronger DBP complex than does uranyl ion and, therefore, the amount of uncomplexed DBP available for raising the equilibrium distribution coefficient for Zr is less in the

Acid-Thorex process. Figure 20 also shows that in the Acid-Thorex process the scrub section flow rate is a more important variable in Zr-95-thorium separation than the DBP content of the scrub section organic phase. It is also apparent that the Zr decontamination factor is not significantly affected by the presence of DBP in the Acid-Thorex process.

CONCLUSION

The decay heat generation and the radiation associated with the fission products in the spent fuel elements affect the fuel reprocessing in both the head-end and the solvent extraction processes. The thermal effect from decay heat generation in the head-end process is primarily on the in-process storage bunkers.

The decay heat in particle bunkers can be adequately removed by any one of the cooling modes discussed earlier provided that the sizing constraints on bunker diameters or bed heights are observed. In the natural convection cooling, the thermal constraint is a function of the maximum allowable centerline temperature and the interstitial gas. The maximum allowable bunker diameter can be greatly extended by using He as the interstitial gas. In the forced convection cooling, the centerline temperature is also a function of bed height. Only a moderate increase in the maximum allowable diameter can be realized with this cooling mode, especially with a tall (3 m) bed. Direct contact internal cooling eliminates the constraint on bunker diameter, and the maximum bed height is a function of the mass velocity of the cooling gas. Since cooling in a fluidized state introduces problems of particle elutriation and filtration, it should be used only when recognizable benefits are obtained by this cooling mode. The internal cooling also increases the burden to the off-gas system unless the cooling gas is recycled.

The models presented may be applied to other types of fuel particles or high-level solid waste storages. However, it is anticipated that criticality constraints in many cases may be more severe than the thermal constraints presented herein.

The radiation effect on the solvent in the Acid-Thorex solvent extraction process, although deleterious, does not pose any significant problem. By using a partition flowsheet (Fig. 18) instead of a coextraction-costrip flowsheet, and by adding fluorides to the 1BX and 1CX columns, an acceptable thorium/uranium partition efficiency has been achieved, and the problem of thorium-DBP and thorium hydroxide precipitates has been eliminated. The loss of Zr DF in the Acid-Thorex process is insignificant compared to that in the Purex process.

ACKNOWLEDGMENTS

The author would like to thank Dr. H. W. Wong* who originally performed the thermal modeling and computation of the particle bunkers. The contributions of G. W. Reddick,** R. G. Wilbourn, and G. E. Benedict in solvent extraction studies are gratefully acknowledged.

---

*Presently employed by EXXON Research and Engineering, Florham Park, New Jersey.

**Presently employed by Rockwell Hanford Operations, Richland, Washington.

This work was supported by the U.S. Department of Energy under Contract DE-AT03-76SF71053.

SYMBOLS

a	surface area per unit bed volume
C_p	specific heat of particles
C_{pg}	specific heat of cooling gas or air
d_p	mean particle diameter
G	mass velocity of cooling gas or air
h	heat transfer coefficient between wall and ambient air or cooling gas
h_c	convective heat transfer coefficient
h_p	heat transfer coefficient between particles and cooling gas or air
h_{rs}, h_{rv}	heat transfer coefficients of thermal radiation between solid surfaces and voids, respectively
H	as defined by Eq. 27
J_o	Bessel function of order zero of first kind
K_e	effective thermal conductivity
K_g, K_s	thermal conductivities of interstitial gas and the solid particle, respectively
L	bed height
N_{Gr}	Grashof number
N_{Pr}	Prandtl number
p	emissivity of bunker wall (taken as 0.2)
Q	volumetric heat generation rate
r	radial position
R	radius of the bunkers
R_o	radius of cylindrical cooling jacket around bunker
t	time
T	temperature
T_a	ambient temperature
T_g	temperature of cooling gas or air
T_g^o	inlet temperature of cooling gas or air
T_{max}	maximum temperature in bed
T_o	initial bed temperature
T_w	wall temperature
x	axial dimension from bottom of cylinder in Fig. 4
α	as defined by Eq. 26
β_m	as defined by Eq. 28
ρ_b	bulk density of particle bed
ε	bed voidage
ϕ	effective thickness of fluid film adjacent to contact surface of two particles = $\phi(\varepsilon, ks/kg)$, given in Ref. 2
μ_g	viscosity of cooling gas or air

REFERENCES

1. McAdams, W. H., Heat Transmission, 3rd Ed., McGraw-Hill Book Co., New York (1954).
2. Kunii, D., and J. M. Smith, "Heat Transfer Characteristics of Porous Rocks," AIChE J1. 6, 71 (1960).

3. Deissler, R. G., and C. J. Eian, "Investigation of Effective Thermal Conductivities of Powders," National Advisory Committee for Aeronautics Report NACA-RM-E52C05, 1952.
4. Schumann, T. E. and V. Voss, "Heat Flow Through Granulated Material," Fuel Sci. Pract. 13, 249 (1934).
5. Argo, W. B., and J. M. Smith, "Heat Transfer in Packed Beds," Chem. Eng. Progr. 49, 443 (1953).
6. Stevens, D. W., "Thermal Conductivity of Beds of Coated Fuel Particles," Nucl. Appl., 3, 626 (1967).
7. General Atomic Company unpublished data.
8. Wong, H. W., ERDA Report GA-A14094, General Atomic Company, "Thermal Analysis of Reprocessing Particle Hoppers," October 15, 1976.
9. Davis, W., Jr., "Radiation Densities and TBP Radiolysis during Thorex Short Decay Runs," Oak Ridge National Laboratory Report, ORNL-2764, 1959.
10. Blake, C. A., Jr., "Solvent Stability in Nuclear Fuel Processing: Evaluation of the Literature, Calculation of Radiation Dose, and Effect of Iodine and Plutonium," Oak Ridge National Laboratory Report, ORNL-4212 (1968).
11. Richardson, G. L., "The Effect of High Solvent Radiation Exposures on TBP Processing of Spent LMFBR Fuels," HEDL-TME-73-51 (June 1973).
12. Dugone, J., "Solvent Degradation," ACC-ICPP-GJS-3-75 (1975).
13. Williams, T. E., and R. W. Wilkinson, "Radiolysis of TBP," Nature, Vol. 179 (1957).
14. Burr, J. G., "The Radiolysis of Tributyl Phosphate," Radiation Research, 8, 214-221 (1958).
15. Burger, L. L., and E. McClanahan, "TBP and Its Diluent Systems," Ind. Eng. Chem. 50, 153-156 (February 1958).
16. Reddick, G. W.,"Solvent Extraction in HTGR Reprocessing, Interim Development Report," ERDA Report GA-A13835, General Atomic Company, February 1976.
17. Wilbourn, R. G.,"Solvent Extraction in HTGR Reprocessing, Interim Development Report II," DOE Report GA-A15030, July 1978.

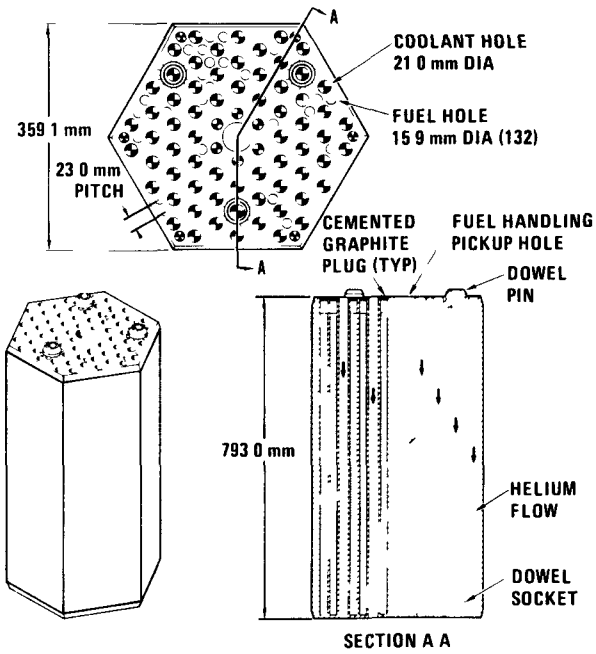

Fig. 1. HTGR standard fuel element

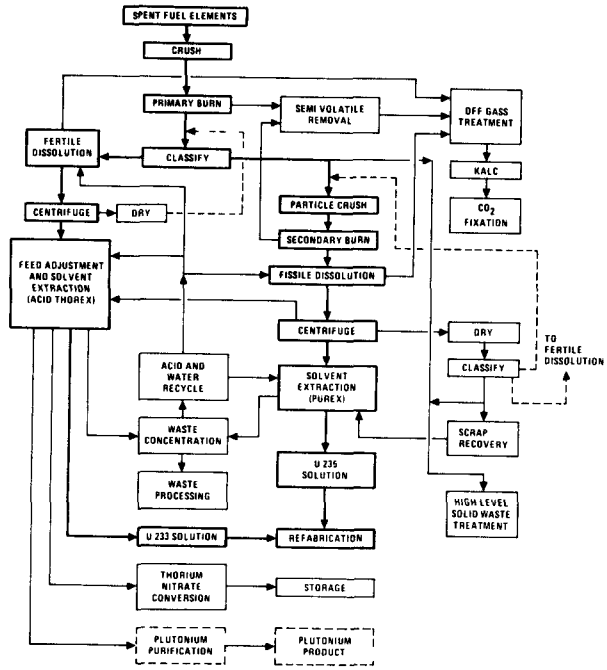

Fig. 2. Reprocessing flow diagram

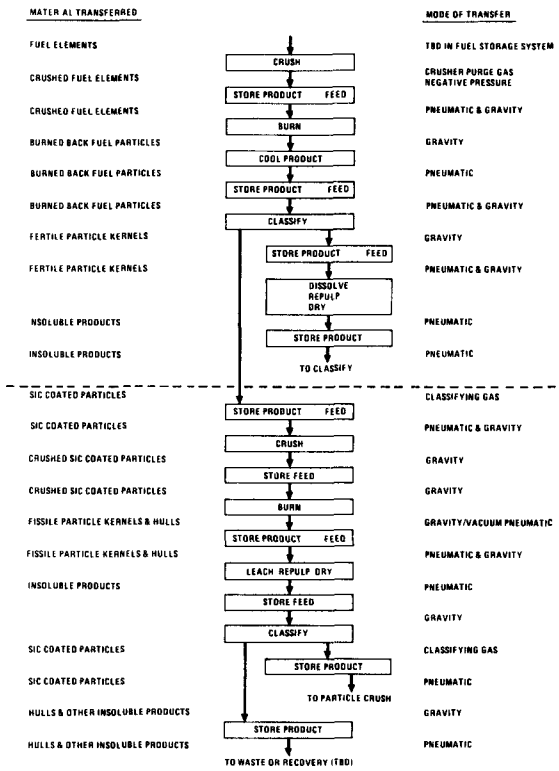

Fig. 3. Transport system routes and storage points

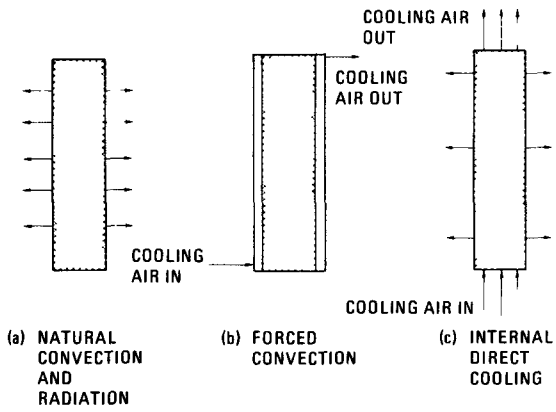

Fig. 4. Three modes of decay heat removal

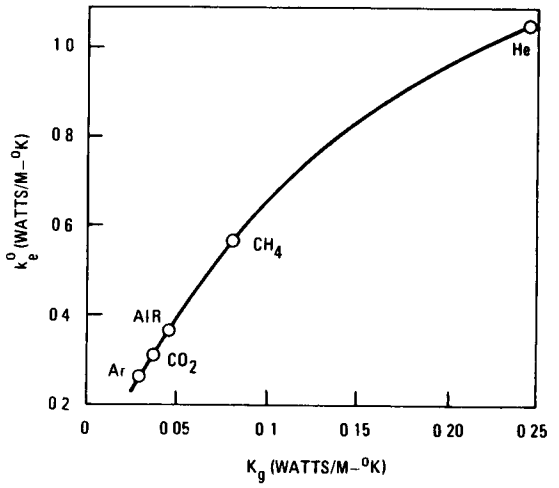

Fig. 5. Sensitivity of k_e^o to k_g for fuel particles at 300°C

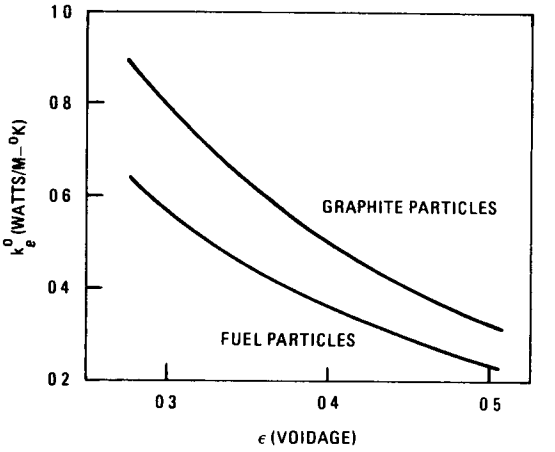

Fig. 6. Sensitivity of k_e^o to voidage

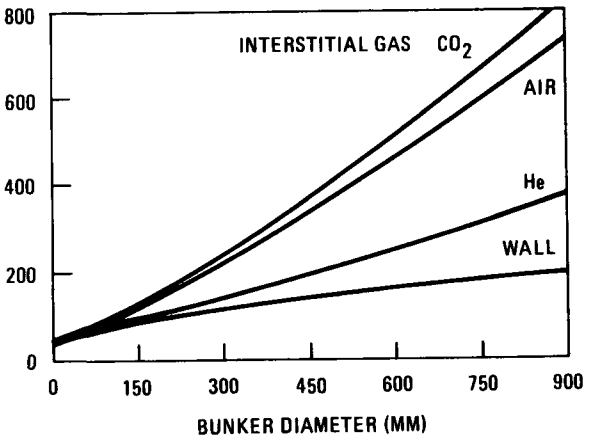

Fig. 7. Centerline and wall temperatures of crushed fuel element particle beds

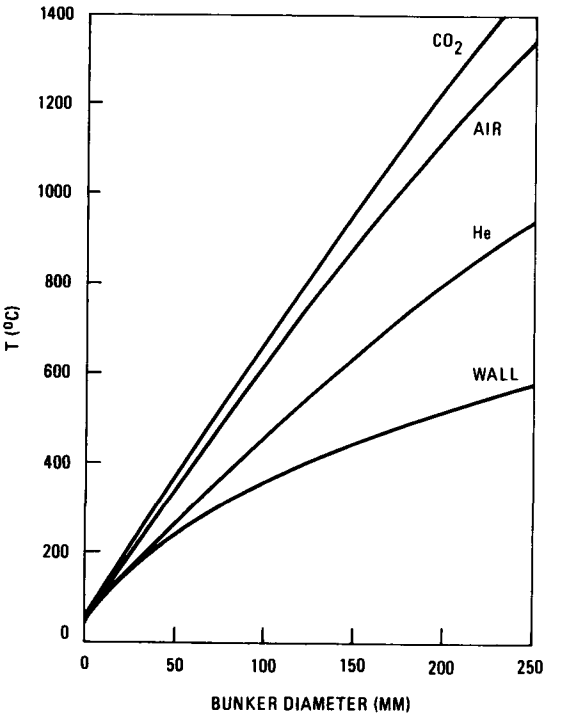

Fig. 8. Mixed fuel particle bed centerline and wall temperatures

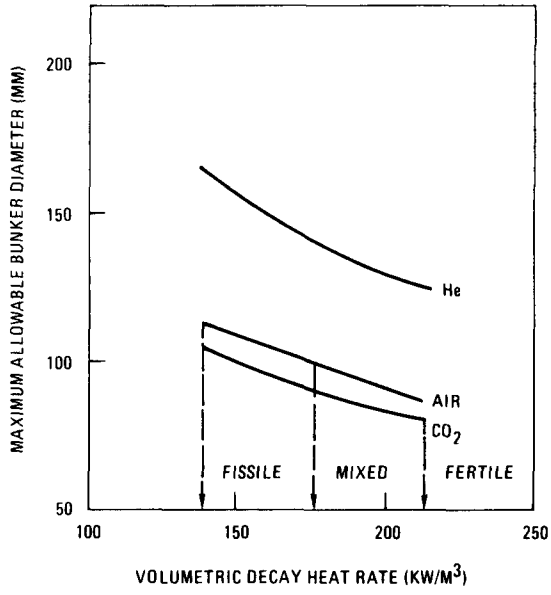

Fig. 9. Maximum allowable bunker diameters for fuel particles

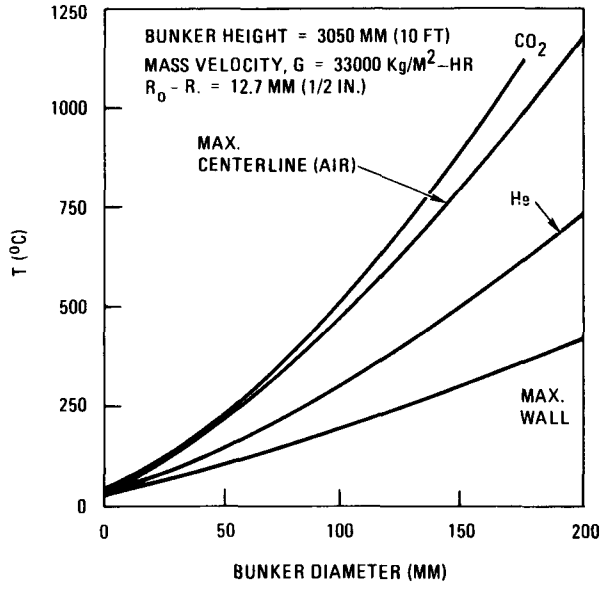

Fig. 10. Maximum centerline and wall temperatures of jacketed mixed fuel particle bunkers

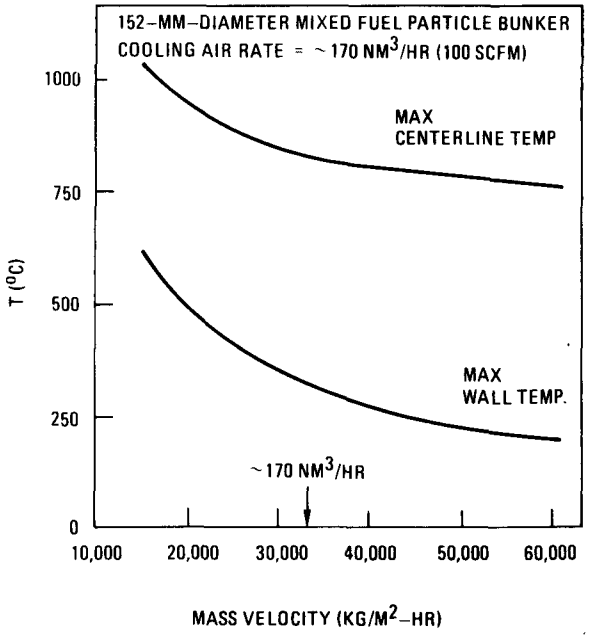

Fig. 11. Effect of cooling air velocity on jacketed bunker temperature for 152-mm-dia mixed fuel particle bunkers

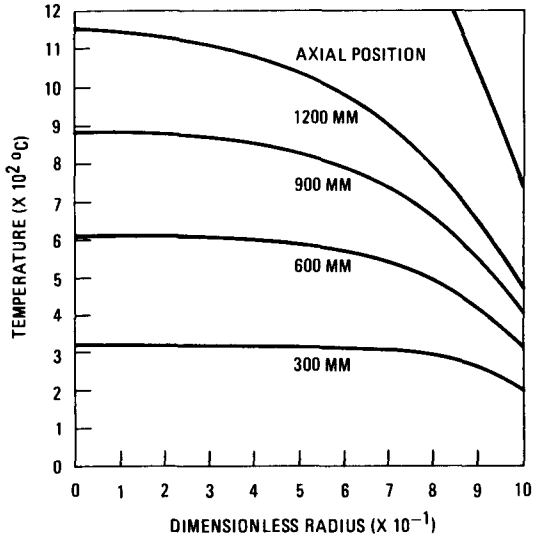

Fig. 12. Radial temperature distribution of mixed fuel particle bed with direct internal cooling

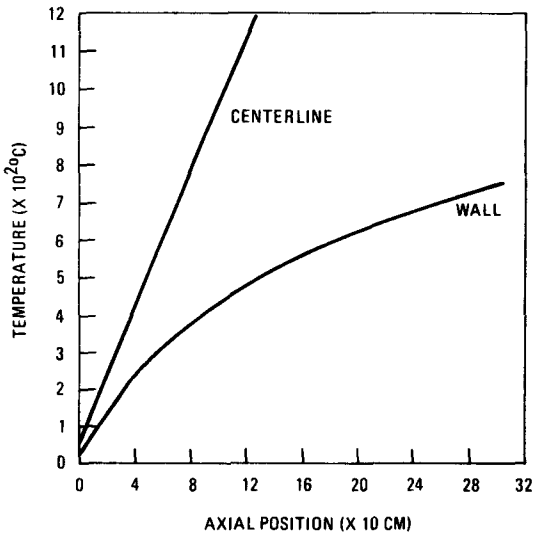

Fig. 13. Axial temp distribution of mixed fuel particle bed with direct internal cooling

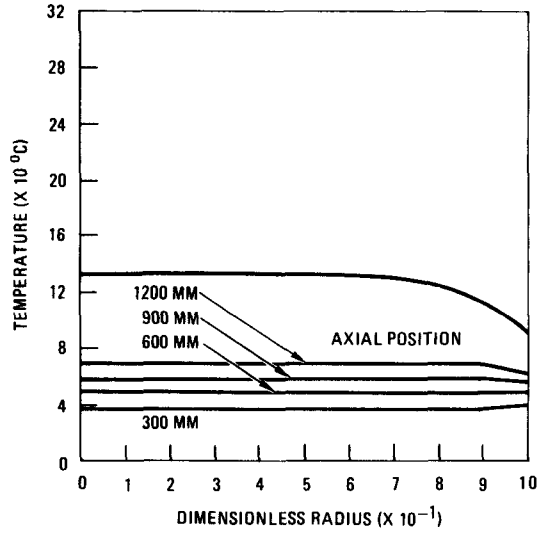

Fig. 14. Radial temp distribution of crushed fuel element bed with direct internal heating

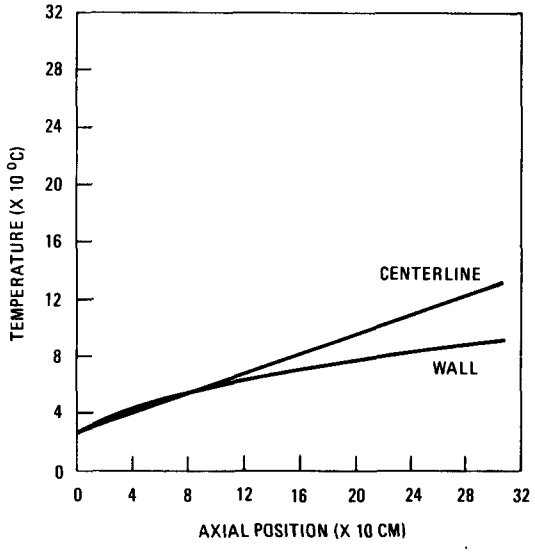

Fig. 15. Axial temp distribution of crushed fuel element bed with direct cooling

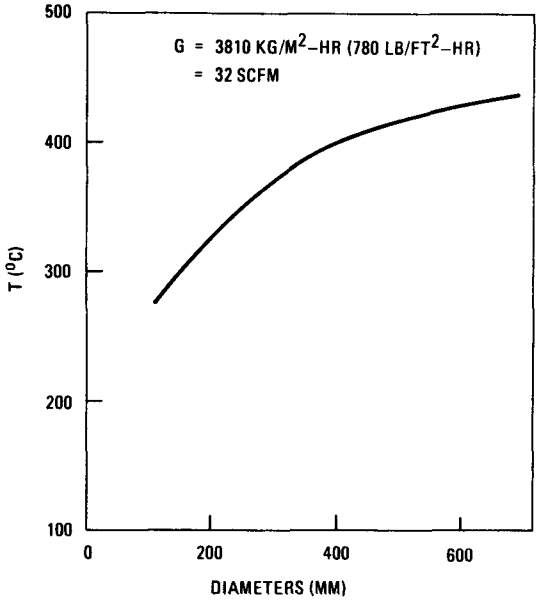

Fig. 16. Equilibrium fluid bed temperatures of mixed fuel particle beds

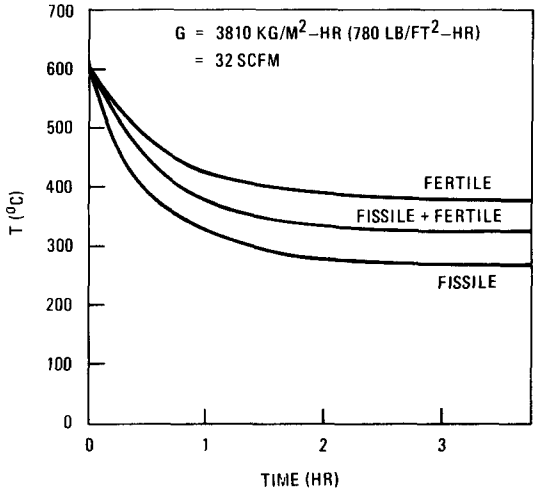

Fig. 17. Transient fluid bed temps of 152-mm-dia fuel particle bunkers

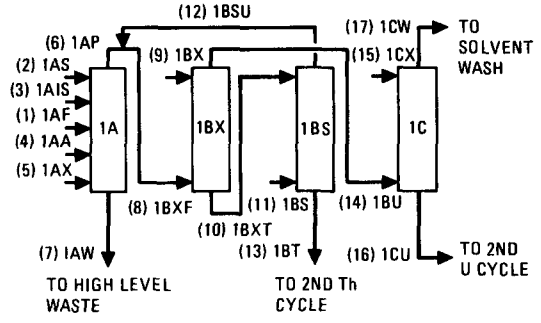

Fig. 18. Acid-Thorex partition cycle flowsheet

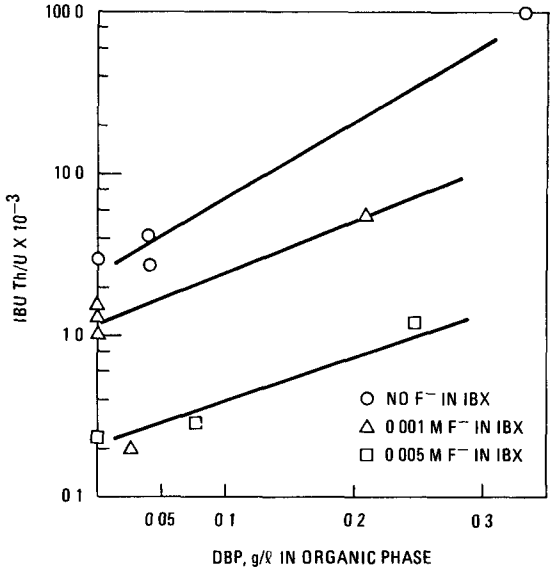

Fig. 19. Effects of fluoride in 1BX stream

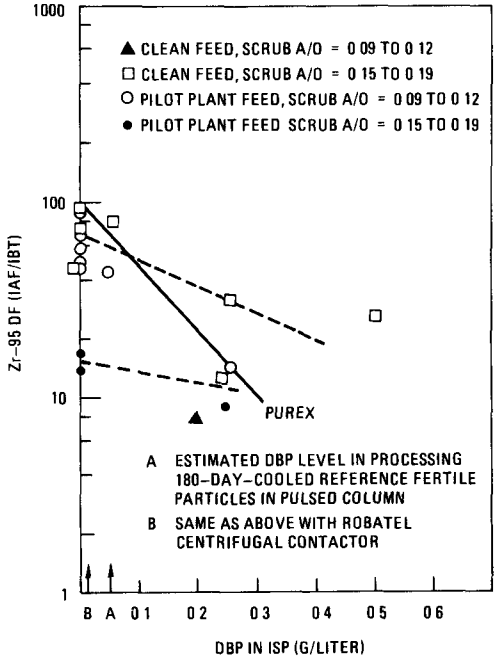

Fig. 20. Measured Zr-95 decontamination factors